Title

Ambient aerosol composition by infrared spectroscopy and partial least squares in the chemical speciation network: Multilevel modeling for elemental carbon

Journal

Aerosol Science and Technology, 52(6)

ISSN

0278-6826

Authors

Weakley, Andrew T
Takahama, Satoshi
Wexler, Anthony S
et al.

Publication Date

2018-06-03

DOI

10.1080/02786826.2018.1439571

Peer reviewed

Aerosol Science and Technology

ISSN: 0278-6826 (Print) 1521-7388 (Online) Journal homepage: http://www.tandfonline.com/loi/uast20

Ambient aerosol composition by infrared spectroscopy and partial least squares in the chemical speciation network: Multilevel modeling for elemental carbon

Andrew T. Weakley, Satoshi Takahama, Anthony S. Wexler & Ann M. Dillner

To cite this article: Andrew T. Weakley, Satoshi Takahama, Anthony S. Wexler & Ann M. Dillner (2018) Ambient aerosol composition by infrared spectroscopy and partial least squares in the chemical speciation network: Multilevel modeling for elemental carbon, Aerosol Science and Technology, 52:6, 642-654, DOI: 10.1080/02786826.2018.1439571

To link to this article: https://doi.org/10.1080/02786826.2018.1439571

Accepted author version posted online: 09 Feb 2018.
Published online: 07 Mar 2018.

AEROSOL SCIENCE AND TECHNOLOGY
2018, VOL. 52, NO. 6, 642–654
https://doi.org/10.1080/02786826.2018.1439571

Ambient aerosol composition by infrared spectroscopy and partial least squares in the chemical speciation network: Multilevel modeling for elemental carbon

Andrew T. Weakley[a], Satoshi Takahama[b], Anthony S. Wexler[a], and Ann M. Dillner[a]

[a]Air Quality Research Center, University of California Davis, Davis, California, USA; [b]ENAC/IIE Swiss Federal Institute of Technology Lausanne (EPFL), Lausanne, Switzerland

ABSTRACT

Fourier transform infrared spectroscopy (FT-IR) has been used to predict elemental carbon (EC) on polytetrafluoroethylene (PTFE) filter samples from the United States Environmental Protection Agency's Chemical Speciation Network (CSN). This study provides a proof-of-principle demonstration of using multilevel modeling to determine thermal/optical reflectance (TOR) equivalent EC (a.k.a., FT-IR EC) on PTFE samples collected in the CSN. Initially, spectra from nine geographically disperse sites were pooled and calibrated directly to collocated TOR EC measurements. The FT-IR EC quantified in test samples was deemed substandard when judged against an earlier study, e.g., $R^2 = 0.760$ and median absolute deviation (MAD) = 26.7%. Upon scrutinizing each sample's absolute prediction error and squared Mahalanobis distance, Elizabeth, NJ predictions were found to exhibit atypical systematic errors, motivating the development of a multilevel classification and calibration procedure. Atypical Elizabeth spectra were distinguished from the (typical) CSN spectra by training a partial least-square discriminant analysis. Predicting EC using calibrations dedicated to either atypical or typical samples produced a satisfactory improvement in overall performance ($R^2 = 0.886$, MAD = 19.8%). Analysis of the atypical FT-IR spectra and select TOR thermal fractions suggested that Elizabeth samples contained elevated levels of diesel particulate matter as evidenced by the use of organic nitrogen functional groups for prediction, very low average OC/EC, and minimal charring during TOR speciation. FT-IR EC from the other eight sites was predominately determined by aliphatic C-H, C = C aromatic, and functional groups associated with oxidation. This study provides preliminary confirmation that FT-IR EC may be accurately determined from source-oriented calibrations under a combined classification and calibration methodology.

ARTICLE HISTORY
Received 9 September 2017
Accepted 5 February 2018

EDITOR
Paul Ziemann

1. Introduction

The United States (US) Environmental Protection Agency's (EPA's) Chemical Speciation Network (CSN) monitors and assesses long-term trends in urban and suburban fine particulate chemical composition ($PM_{2.5}$, < 2.5 μm aerodynamic diameter) (Hand et al. 2013; Solomon et al. 2014). Atmospheric $PM_{2.5}$ comprises a complex mixture of all organic and inorganic condensed-phase material emitted from primary anthropogenic and biogenic sources, generated in the atmosphere by secondary gas-to-particle inter-conversion processes, or formed within the particle-phase according to second-generation "aging" mechanisms (Kanakidou et al. 2005; Hallquist et al. 2009; Kroll et al. 2015). Although our ability to measure, evaluate, and predict the composition and evolution of $PM_{2.5}$ remains a challenge (Kroll and Seinfeld 2008), the net effect on visibility (Watson 2002; Malm and Hand 2007), climate forcing (Pöschl 2005; Fuzzi et al. 2015), and human health (Pope III and Dockery 2006; Anderson et al. 2012) warrant continued elucidation of $PM_{2.5}$ constituents by state-of-the-art measurement techniques and models.

Organic and elemental carbon (OC and EC) are two pollutants measured in the CSN using the IMPROVE_A thermal/optical reflectance (TOR) method (Chow et al. 1993, 2007). Aerosol speciation by the TOR method is minimally selective, i.e., all semi- and low-volatility carbon evolving from the quartz filter in an inert atmosphere is assigned as OC (140°C–580°C) while non-volatile (refractory) carbon evolving after oxidation is defined as EC (>580°C; 98%/2% He/O_2). TOR OC therefore describes a mixture of hundreds or thousands of compounds with no direct access to molecular composition or solution properties (e.g., functionality, solubility).

CONTACT Ann M. Dillner amdillner@ucdavis.edu Crocker Nuclear Laboratory, University of California Davis, Davis, CA 95616, USA.
Color versions of one or more of the figures in the article can be found online at www.tandfonline.com/uast.

Likewise, TOR EC is assumed to be comprised of a mixture of graphitic carbon species, of varying degrees of oxidation, with the architects of thermal/optical analysis intending to estimate the soot carbon fraction of atmospheric samples (Huntzicker et al. 1982; Gundel et al. 1984; Novakov and Rosen 2013). Potential biases in thermal analysis (EC) and optical (BC) analysis—not connected to analysis artifacts—are addressed in Andreae and Gelencsér (2006) and more recently by Petzold et al. (2013) and Lack et al. (2014). Where artifacts in thermal /optical analysis are concerned, multi-wavelength methods are beginning to systematically address biases associated with light absorbing brown carbon (= OC) being incorrectly assigned as EC (Massabò et al. 2016). However, the historical significance of TOR EC measurement and its role as a "standard" measurement is important to consider. For instance, thermal optical measurement of EC, though slightly different from the TOR protocol but containing a similar class of artifacts, was recently adopted by the European Committee for Standardisation (CEN) Technical Committee 264 (standard method EN 16909:2017).

Therefore, within the broader scope of providing rapid and non-destructive chemical characterization from polytetrafluoroethylene (PTFE) filters typically used for gravimetric mass measurement, TOR OC and EC were predicted in ambient fine aerosols using Fourier transform infrared (FT-IR) spectroscopy and a multivariate partial least-square (PLS) regression for the CSN and Interagency Monitoring of PROtected Visual Environment (IMPROVE) network (Coury and Dillner 2008; Ruthenburg et al. 2014; Dillner and Takahama 2015a, 2015b; Takahama et al. 2016; Weakley et al. 2016). The TOR equivalent OC and EC mass concentrations estimated by FT-IR—herein denoted FT-IR OC and EC—are accurate, precise, and repeatable across time and location in a given network. Calibrating TOR concentrations directly to parallel FT-IR measurements produces regression parameters robust to interference from the PTFE sampling filter and non-carbonaceous mixed aerosol species. For example, FT-IR OC calibrations developed from only six geographically dispersed IMPROVE sites were extended to filters collected during different years and sites (Reggente et al. 2016). This provided evidence that OC quantification using only a single ("global") PLS calibration may remain viable in the long run. However, IMPROVE EC calibrations are not as readily extrapolated to filters obtained from different sites suggesting that certain sites exhibiting more "atypical" spectra may benefit from their own dedicated EC calibration(s).

Addressing any apparent limitations of FT-IR EC quantification is a particularly pressing matter as technological change and policy continue to modify sources, atmospheric processing, and the ultimate fate of carbonaceous aerosol in the urban and rural environment (Hallquist et al. 2009; Johnson 2009; Shindell et al. 2012; Zhao et al. 2013). The capability for FT-IR to provide TOR-equivalent EC among other quantities—TOR-equivalent OC (Weakley et al. 2016) and functional groups (Takahama et al. 2013; Ruthenburg et al. 2014)—from a single PTFE filter spectrum can be useful when quartz filters for TOR analysis are not available. The goal of this work is to develop a framework for measuring EC in diverse sites using FT-IR spectra given the chemical variability of EC. As a practical matter, the long-term viability of the FT-IR method depends on an ability to distinguish atypical from more typical EC given only knowledge of a sample's infrared spectrum. The first task of the current study aims to identify atypical and typical samples using absolute prediction errors and each spectrum's squared Mahalanobis distance. As a move toward using only spectral information for distinguishing sample types, CSN spectra are then classified as containing either "atypical" or "typical" EC using a partial least-square discriminant analysis (PLS-DA; Barker and Rayens 2003). Samples dichotomously classified by PLS-DA are then assigned to their respective "atypical" or "typical" calibrations. Combining classification and FT-IR EC prediction in this manner will be referred to as multilevel EC modeling. Validation next concerns comparing multilevel EC predictions to EC predicted from a single calibration (where all samples are predicted using a single "global" calibration). Given demonstrable reduction in EC prediction errors by multilevel quantification, the spectroscopic and thermal/optical behavior of atypical samples are evaluated to ascertain the underlying differences that distinguish atypical from typical behavior in prediction. Overall, this study assesses the efficacy of combining classification and calibration to determine FT-IR EC in PTFE samples from US aerosol monitoring networks.

2. Methods

2.1. Sampling and analysis in the CSN

Samples were acquired from 10 CSN sites (2013 sampling year) located within or near the following cities: Birmingham, AL, Boston, MA, Cleveland, OH, Elizabeth, NJ, Fresno, CA, Phoenix, AZ, Providence, RI, Salt Lake City, UT, Seattle, WA, and Washington, DC. The Boston and Cleveland sites have two collocated CSN samplers. Samplers were configured to collect ambient aerosol for 24 h (midnight to midnight) on both PTFE (Whatman $PM_{2.5}$ membranes, 47 mm) and quartz filters (Pall, 25 mm). Quartz filters were used for TOR analysis. PTFE filters were used for gravimetric mass, elemental

analysis using X-ray fluorescence (XRF), and FT-IR analysis. SASS samplers (MetOne, Grant's Pass, OR, USA) were configured to pass 6.7 liters per minute of ambient air through PTFE filters resulting in 9.65 m^3 of total air sampled. The URG-3000N (URG, Chapel Hill, NC, USA) sampler passed ambient air though quartz filters at 22 liters per minute resulting in 31.7 m^3 of total air sampled. All samples were shipped and stored cold (4°C). The quartz filters were shipped for TOR analysis at the Desert Research Institute (Reno, NV, USA) and the PTFE filters were first shipped to Research Triangle Institute (Research Triangle Park, NC, USA) for gravimetric and XRF analysis. FT-IR analysis was performed at the University of California, Davis (Davis, CA, USA).

Collocated quartz sampling at two CSN sites facilitated a quality assessment of the TOR measurements prior to FT-IR calibration. Here, the integrity of the TOR data was assessed for drift that may have occurred as a result of instrument malfunction, poor sampler maintenance, or reasons unknown. The methods used to establish the quality of TOR samples can be found in Weakley et al. (2016). After quality assessment, samples from the Birmingham and one of the collocated Cleveland sites were determined to be substandard due to excessive drift. Nine sites were therefore retained for PLS modeling leaving 927 total samples containing 30 field blanks for calibration and prediction. Twenty-nine collocated samples from Boston were used to estimate errors related to aerosol sampling and TOR analysis.

2.2. TOR EC measurements

TOR EC measurements were acquired from the EPA's Air Quality System (AQS) database on July 27, 2015 (https://aqs.epa.gov/api). During TOR analysis the carbonaceous compounds leaving the quartz filter are converted to CO_2, methylated, and the products passed to a flame ionization detector (FID). Although thermal speciation is continuous during TOR, the formation of unwanted organic pyrolysis products (OP; "char") is minimized by fractionating OC according to four temperature set points—designated OC1, OC2, OC3, and OC4 on analysis thermograms (Chow et al. 2007).

Char formation is rarely eliminated by fractionation alone, with OP remaining bound to filter media until the addition of oxygen that defines the first EC fraction (EC1). Distinguishing the OP artifact from real aerosol species contained in EC1 involves monitoring the reflectance of a helium-neon (633 nm) laser off the quartz filter during thermal analysis. Specifically, a continuous drop in He-Ne reflectance is often observed during the OC fractionation process. This decrease in reflectance signifies the formation of OP since char is characteristically more light absorbing than OC precursor compounds. After OC4 fractionation, oxygen introduced into the chamber causes both char and EC to oxidize whereby sample reflectance increases rapidly. When sample reflectance returns to its initial value, it is assumed that all nascent OP artifacts have been removed leaving only refractory aerosol species on the filter. OC, OP, and EC are then determined by analysis of the TOR thermograms with total OC equal to the sum of the OC fractions and OP (OC = OC1+OC2+OC3+OC4+OP) and EC the sum of the EC thermal fractions less OP (EC = EC1+EC2+EC3-OP). TOR OC and EC measurements are reported on the AQS database as mass concentrations ($\mu g/m^3$).

2.3. FT-IR analysis

Absorption spectra of PTFE filters were acquired on the Bruker Tensor 27 FT-IR spectrometer (Bruker Optics, Billerica, MA) equipped with a liquid nitrogen cooled mercury-cadmium-telluride detector. Measurements were acquired in transmission mode with the infrared beam interrogating the center of the PTFE filter. Instrument parameters included collection at 4 cm^{-1} nominal resolution (aperture diameter = 6 mm) with a spectral range from 4000 cm^{-1} to 420 cm^{-1} (2.5–24 μm). The sampling compartment was dry air purged of both water vapor and carbon dioxide for 4 min prior to acquiring a background spectrum (PureGas LLC, Broomfield, CO, USA). Absorbance spectra were calculated after ratioing a single beam spectrum of the empty sample compartment against the filter spectrum. The precise details of FT-IR collection can be found in Ruthenburg et al. (2014).

Ambient aerosol and the PTFE filter both attenuate infrared radiation by three primary mechanisms: absorption, scattering, and specular reflection. Scattering and reflection by the PTFE filter fibers, and to a lesser extent the collected aerosol, introduce a very broad baseline and offset in the infrared spectra that is superimposed on the much narrower absorption bands. Estimating and removing baseline from the spectra is accomplished in this study using the smoothing splines baseline correction method (Kuzmiakova et al. 2016). Default parameter selection criteria were used to select the optimal effective degrees of freedom (= 2). Furthermore, the smoothing spline method also truncates spectra at ~1426 cm^{-1} thus assuming that any aerosol bands <1426 cm^{-1} are either totally or partially confounded by PTFE (Liang and Krimm 1956). Baseline corrected and truncated spectra therefore contain a total of 2002 absorption measurements available for EC calibration.

Each TOR measurement (y) and matching spectrum ($[X]$) is next sorted by site and date. Calibration and test

samples are then partitioned by placing every third sample-pair in the test set (for validation) with the remaining two thirds in a calibration set (for model training). Partitioning samples in this way aims to produce single-model EC predictions that are insensitive to any sample-to-sample variations in aerosol composition that may be linked to seasonality and/or a host of other factors inaccessible by FT-IR and TOR analysis (e.g., sources, mixing state). Placing every third sample in the test set ensures that the same factors are represented during model validation. Partitioning results in 588 samples for calibration and 329 samples for method testing.

2.4. FT-IR EC: Single and two-model prediction

2.4.1. FT-IR EC predictions using a single calibration

An FT-IR calibration was first developed from all available calibration samples, making no distinction between atypical or typical EC, in an effort to identify and then evaluate to what extent atypical samples degrade EC predictions ($N = 588$). First, developing and validating FT-IR calibrations of this type has been extensively covered in previous work (Dillner and Takahama 2015b; Weakley et al. 2016). An abridged version of model development and validation is therefore presented. First, the number of PLS components used for calibration are selected according to a minimized root-mean-square error of five-fold cross-validation (Arlot and Celisse 2010). Regression coefficients ($\hat{b}$) are then estimated using the nonlinear iterative partial least-square (NIPALS) algorithm (Wold et al. 2001). Note that an additional optimization step was applied to the calibration using backward Monte Carlo unimportant variable elimination (BMCUVE) to identify only the wavenumbers considered absolutely essential to determine EC (Weakley et al. 2014).

FT-IR EC mass-concentrations are simultaneously determined in the 329 test samples by matrix multiplying test spectra by regression coefficients ($y_{FTIR} = [X]\hat{b}$). Prediction errors, $e = y_{FTIR} - y_{TOR}$, are next used to judge model performance on six figures of merit including: R^2, median absolute error, concentration-normalized median absolute deviation (MAD, %), concentration-normalized bias (%), minimum detection limit (MDL), and precision. Field MDLs were estimated as three times the standard deviation of predicted test set blanks (Committee 1987). Duplicate precision was estimated from FT-IR EC determined from collocated Boston samples.

Determining FT-IR EC using two independent models (atypical and typical) is only considered worthwhile if the figures of merit for single-model predictions are considerably worse than previously reported (Dillner and Takahama 2015b; Reggente et al. 2016). Given that previous IMPROVE studies collected aerosol on PTFE filters with the (nominal) mass per square centimeter roughly 10–11 times greater than these CSN samples (McDade et al. 2009), only mass-normalized figures of merit metrics are used to judge a calibration's performance. Namely, a calibration showing an $R^2 > 0.85$, normalized bias $< |3|$%, and normalized error <25% is considered an acceptable model.

2.4.2. Identifying atypical EC

Reggente et al. (2016) demonstrated that atypical and typical samples are distinguishable by plotting squared Mahalanobis distance (D_i^2) against absolute prediction error ($|e_i|$). Conceptually, plots developed from these metrics constitute a two-dimensional map, useful in evaluating a spectrum's degree of dissimilarity to the other test spectra (D_i^2) and whether the dissimilarity is associated with poorer EC predictions ($|e_i|$). Samples are judged as poorly predicted if they exceed the spectrum dissimilarity threshold defined by absolute errors exceeding 3.5 times the mean absolute error of calibrated EC ($|e_i| > 3.5\ \overline{|e|}$) and squared Mahalanobis distance exceeding three times that of the mean calibration spectrum ($D_i^2 > 3\ \overline{D^2}$).

For the CSN samples used in this study, atypical samples are poorly predicted by the single EC calibration but *do not* exceed the spectra dissimilarity threshold. In other words, the expectation that only *major* differences in FT-IR absorption bands yield poor predictions (e.g., due to interferences or matrix effects) are not apparent in atypical samples, implying that *subtle* differences in the EC composition must distinguish atypical spectra from more typical ones. Moreover, since differences in FT-IR spectra between atypical and typical samples are slight, they are only distinguishable by taking into account the relationship between predicted values and TOR reference measurements (y_{TOR}).

Figure 1a identifies most atypical samples as collected from the Elizabeth, NJ monitoring station. Specifically, Elizabeth, NJ spectra show no major differences in infrared absorption according to the squared Mahalanobis distance ($D_{i,NJ}^2 < 3\ \overline{D^2}$) but many EC predictions fall above the estimated absolute error threshold (Figure 1a). Upon further inspection, Elizabeth, NJ EC predictions actually become increasingly less accurate as the mass of aerosol on the filters increases (Figure 1b). This regression behavior signifies that systematic differences— possibly linked to EC composition—exist between Elizabeth, NJ samples and those from the other eight sites. As hypothesized above, a calibration dedicated exclusively to atypical samples (Elizabeth, NJ, USA) should control for the effect of aerosol composition in a multilevel modeling framework.

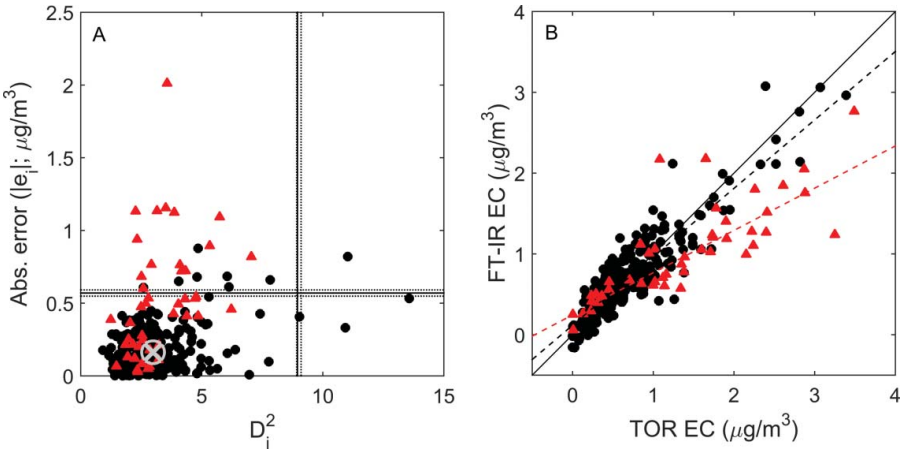

Figure 1. Each FT-IR test spectrum's squared Mahalanobis distance (D_i^2) plotted against absolute error ($|e_i|$; a) and cross plot comparing FT-IR predictions to TOR EC (b). Elizabeth, NJ samples are distinguished from the other eight sites as triangles (red) in both plots. Boundaries and complementary 95% confidence intervals were calculated as three times the mean-squared Mahalanobis distance and 3.5 times mean absolute error of the calibration samples, denoted as an encircled X (a). Dashed lines (b) qualify the systematic deviation in Elizabeth, NJ samples from the other eight sites via robust least-square regression.

Figure 1 exposes atypical behavior in several CSN samples; most of which are Elizabeth, NJ samples. Therefore, we first hypothesize that atypical behavior stems exclusively from heterogenous soot on Elizabeth, NJ samples. Two calibrations are therefore developed: one for Elizabeth, NJ samples (= atypical EC) and another for typical EC from the other eight sites (= typical EC). Figure 1b in particular demonstrates that this approach to multilevel modeling is altogether justified: Elizabeth predictions appear to *systematically* deviate from the other eight sites down to 0 $\mu g/m^3$, i.e., absolute prediction errors scale with the mass of ambient aerosol on Elizabeth filters. This implies that most Elizabeth, NJ EC is likely atypical but that atypical behavior is not detectable below ~2 $\mu g/m^3$ in Figure 1a. Furthermore, if multilevel predictions, performed by developing a calibration for Elizabeth EC separately from the other eight sites, are judged sufficient this provides evidence as to the validity of multilevel modeling along these lines (see Section 2.4.1). Finally, if the wavenumbers used for a Elizabeth quantification are plausibly connected to aerosol sources distinct from typical samples, this provides support for our hypothesis that atypical Elizabeth EC is chemically different from typical EC.

2.4.3. Two-model predictions

After distinguishing atypical from typical samples, data partitioning for calibration and method testing is again performed. Typical samples are partitioned at a 2-to-1 ratio (identical to the single-model case) with 528 and 298 samples in the calibration and test set, respectively. Atypical samples are partitioned at an approximately 1-to-1 ratio with 46 used for calibration and the other 45 were for validation. Partitioning atypical samples in this manner ensures that uncertainties related to low sample number in figures of merit are minimized to the extent possible. Overall, the combined training and test sets contain a total of 574 and 343 samples, respectively.

A PLS-DA classifier is next trained to assign a test spectrum to an appropriate model for EC quantification (Figure 2). Training and validating the PLS-DA classifier requires first coding each calibration sample's true affiliation as either "atypical" or "typical" using numeric class labels. Atypical samples were assigned a value of +1 and typical samples were assigned -1. Class labels corresponding to calibration samples were then placed in a vector and matched to their respective FT-IR spectra. Our variant of PLS-DA divides classification into two distinct steps. First, the FT-IR spectra are regressed onto the vector of class labels using the NIPALS algorithm. Second, the PLS scores (e.g., t_1 and t_2) derived from the PLS regression are used to estimate class-conditional (normal) probability densities, equivalent to defining the linear discriminant boundary shown in Figure 2a (Dixon and Brereton 2009; Hastie et al. 2009). In this context, the PLS scores are estimated as a linear combination of the FT-IR absorption measurements with the combination coefficients (a.k.a, PLS components) determined by considering the covariance between the spectra and class labels (see Takahama et al. 2016 for detailed description of the PLS algorithm applied to ambient aerosol spectra). Geometrically, the PLS components project FT-IR spectra onto a low-dimensional basis prior to performing discriminant analysis or regression. The PLS scores contain the coordinates of each spectrum in this new basis. For example, Figure 2a illustrates a mapping of each spec-

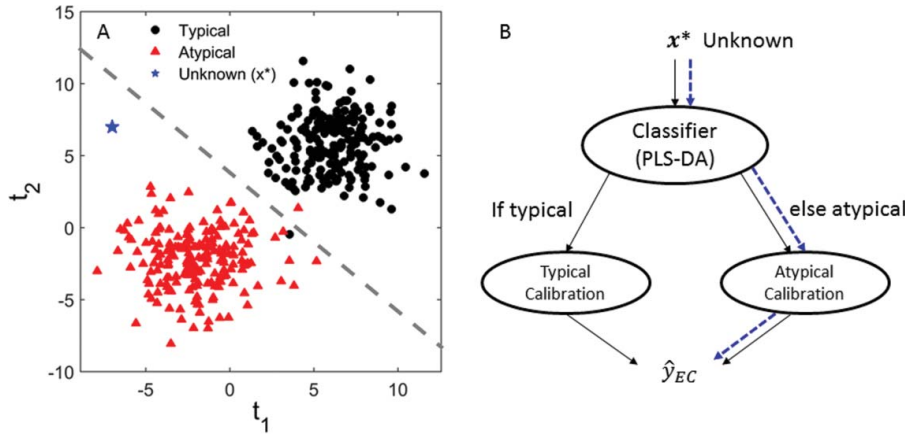

Figure 2. Example of classifying an unknown spectrum (x^*) as either atypical or typical using PLS-DA (a). In this context, the PLS scores (t_1 and t_2) may be thought of as transformed FT-IR spectra where each point represents a spectrum, distinguished here according to class label. For the purpose of this illustration, 200 atypical and typical samples were simulated from two Gaussian distributions with a mean of (−2, −2) and (6,6), respectively. Simulated class variances are equal ($\sigma_{ii}^2 = 4$, $\sigma_{ij}^2 = 0$). Estimating the mean of each class and pooled-covariance matrix defines the boundary used to classify and then allocate an unknown test spectrum (star; a) to the appropriate FT-IR calibration (dashed path; b).

trum—which originally contains up to 2002 absorption measurements in smoothing spline spectra—onto a set of coordinates, t_1 and t_2, which are the first two PLS components. Practically speaking, performing discriminant analysis using the PLS scores instead of the FT-IR spectra ensures that a suitable solution is found, given that the PLS scores are free from the excessive collinearity in the spectra (Næs and Mevik 2001).

Once this boundary has been estimated from calibration samples, test samples are then classified as either typical or atypical depending on their position relative to the boundary. Depending on the number of transformed variables used for analysis, the boundary may be a line (as in Figure 2a), plane (three variables), or hyperplane (>3 variables). In the current study, the number of variables chosen for PLS-DA was determined according to a minimized five-fold cross-validated misclassification rate.

Following test sample classification, atypical and typical calibrations are developed individually using the same sequence of steps for single-model development, i.e., samples are partitioned into calibration and test sets, cross-validation is performed to determine model complexity, PLS parameters are estimated, and predictions are validated across six figures of merit (e.g., R^2). Again, each model is optimized using BMCUVE. Optimization is used not only to improve EC predictions but more importantly to elucidate the absorption bands most useful for atypical and typical EC quantification.

2.5. Chemometric and statistics software

The Matlab™ base, statistics toolbox, and signal processing toolbox were used for most data manipulation and visualization purposes (2015a, The MathWorks, Inc., Natick, MA, USA). The NIPALS algorithm and single-pass MCUVE filter function were available from the open-source libPLS package (v1.9, Changsha Nice City, China). The BMCUVE wavenumber selection protocol was programmed by the authors.

3. Results and discussion

FT-IR EC is not accurately determined using only a single PLS calibration (Table 1, Single). Relative to an earlier IMPROVE network study (Hybrid model from Dillner and Takahama 2015b in Table 1), the R^2, bias, MAD, and % below MDL are all unacceptable. Taken together with Figure 1 (above), comparing FT-IR EC to TOR EC reference measurements sufficiently motivates

Table 1 . FT-IR EC determined using either the single or multilevel model. MDLs were determined separately for the typical and atypical calibrations with the later not estimable given only one test set blank classified as atypical.

Model	R^2	Bias (%)	Error ($\mu g/m^3$)	MAD (%)	MDL ($\mu g/m^3$)	% below MDL	Precision ($\mu g/m^3$)
Single	0.760	5.2	0.13	26.7	0.37	24.2	0.08
Multilevel	0.884	2.7	0.11	19.8	[0.17, –]	[4.8, –]	0.04
Hybrid model Dillner and Takahama (2015b)	0.956	−2.6	—	19.5	—	0.7	—

identifying, classifying, and then independently determining atypical and typical EC. As visualized in Figure 1b, FT-IR EC is over-predicted in Elizabeth, NJ samples below 1 $\mu g/m^3$ and then increasingly under-predicted suggesting that the PLS regression parameters (e.g., $\hat{b}$) for most CSN sites are inappropriate for Elizabeth, NJ samples. Non-Elizabeth EC shows only a small deviation from the 1:1 line.

Figure 3 summarizes multilevel EC predictions as well as the classification accuracy of PLS-DA. First, PLS-DA does not misclassify any typical samples as atypical (sensitivity = 100%,) but does misclassify seven atypical samples as typical (specificity = 84%). All incorrectly classified Elizabeth, NJ samples fall within the scatter of the typical samples suggesting that misclassification has a negligible influence on regression figures of merit (Figure 3a). As shown in Figure 3b, the atypical EC samples from Elizabeth, NJ are no longer biased when determined by their own dedicated calibration.

Multilevel EC modeling dramatically improves prediction accuracy (Table 1, Multilevel), confirming that misclassifying some atypical Elizabeth, NJ samples as typical does not noticeably affect EC quantification. In fact, the multilevel model performs comparably to the hybrid IMPROVE model, with the notable exception of R^2 and possibly the percentage of samples below MDL. Given that a more "reasonable" R^2 is observed for the hybrid IMPROVE calibration ($R^2 = 0.956$) while prediction errors are nearly identical to the multilevel model developed in this study (MAD = 19.5% vs. 19.8%), it seems plausible that the lower R^2 in the multilevel model is likely connected to the roughly 10–11 times lower aerosol mass-per-filter area on CSN (PTFE) filters relative to filters collected in the IMPROVE network.

Rather than pooling predicted test set blanks to calculate a single MDL for the multilevel model, we chose to calculate an MDL for the atypical and typical calibrations separately. Under this particular framework of multilevel modeling, a pooled MDL is not theoretically suitable given that each calibration (presumably) utilizes infrared absorption related to potentially distinct aerosol EC (discussed below). By virtue of this, we expect that the probability of correctly distinguishing FT-IR EC from background in an unknown field sample (definition of MDL) is strongly controlled by the composition of EC on a sample as used by each calibration. Therefore, the differences in aerosol composition/absorption used by each calibration require their own dedicated MDLs and a range for the MDL should, in principle, be reported for the multilevel model. However, because there was only one blank classified as atypical, an MDL and % below MDL are not calculable nor reported in Table 1.

3.1. Infrared band assignments for typical calibration

Figure 4 shows a typical CSN spectrum and PTFE field blank overlaid on all spectra collected for this work. The wavenumbers selected by the BMCUVE algorithm for calibration are indicated by vertical bars. Bands used in the typical CSN calibration between 3400 and 3200 cm^{-1} are assigned to several broad and unresolved modes. N-H stretches, from either primary and/or secondary amines (3400–3250 cm^{-1}) as well as hydrogen-bonded and/or conjugated O-H stretches (3300–3200 cm^{-1}) possibly connected to oxidized soot are all plausible assignments in this range (Akhter et al. 1985a; Shurvell 2002).

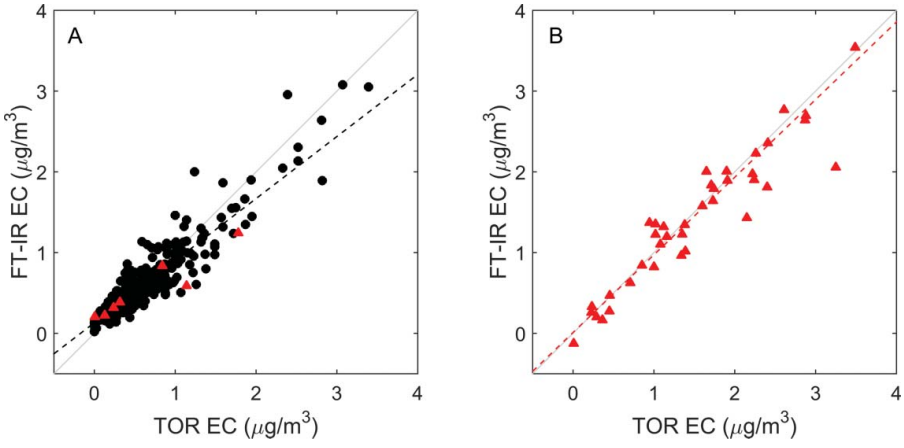

Figure 3. TOR EC plotted against FT-IR EC for typical (a) and atypical (b) model predictions. Typical samples and atypical samples are distinguished as bullets (black) and triangles (red), respectively. Seven atypical Elizabeth, NJ samples were misclassified as typical explaining their affiliation with the typical model (a). No typical samples were misclassified as atypical (b). Dashed lines are calculated using robust least squares and qualify any systematic deviations present in either model's predictions.

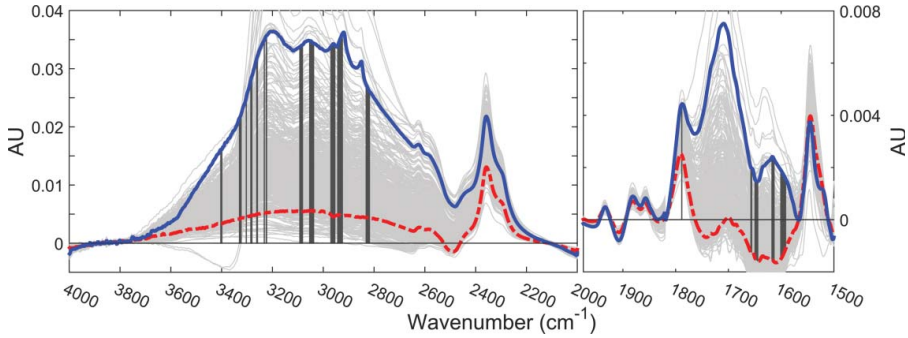

Figure 4. Typical CSN spectra (light gray). A representative typical CSN spectrum (solid line; blue), PTFE blank (dashes; red), and wavenumbers used for calibration (vertical bars) are designated. Note, negative absorption is an artifact of baseline correction. Thicker vertical bars indicate that several adjacent wavenumbers were chosen for calibration.

More confident assignments include the C-H stretches from aliphatic and aromatic functional groups between 3100 and 2800 cm^{-1} (Shurvell 2002). Specifically, absorption concentrated around 3090 cm^{-1} and 3050 cm^{-1} are assigned to aromatic C-H stretches, the former showing some prominence in certain substituted polycyclic aromatics identified in combustion soot (e.g., 1-methyl-pyrene) (Russo et al. 2014). Features between 3000 and 2800 cm^{-1} are assigned to aliphatic C-H stretches associated with multiple functionalities. Antisymmetric stretching of CH_3 and CH_2 (2960 cm^{-1}; 2930 cm^{-1}) as well as CH_2 symmetric stretching (2830 cm^{-1}) are assigned to absorption in this range (Shurvell 2002). Symmetric CH_2 stretches in normal and branched alkanes are usually confined to a fairly narrow wavenumber range at 2850 $\pm$ 10 cm^{-1}, this being 10–20 cm^{-1} higher than the wavenumbers used in the calibration (Mayo 2004a). Interestingly, CH_2 symmetric stretching at 2830 cm^{-1} has been assigned to saturated five- and six-member ring species (e.g., 1,2,3,4-tetrahydronapthelene) in combustion soot and condensed polycyclic aromatics rich in naphthalenic moieties (Russo et al. 2014; Gargiulo et al. 2015). Alternatively, a C-H stretch associated with amines may be assigned to 2830 cm^{-1} with frequency lowering attributed to the Bohlmann effect (Chen et al. 2007).

Absorption spanning 1600–1591 cm^{-1} is plausibly assigned to graphitic C = C stretches and has been identified previously in the spectra of combustion soot and model elemental carbons (Akhter et al. 1985b; Kostić et al. 2009; Lechner et al. 2016). However, a few qualifications regarding this assignment are necessary. First, non-graphitic aromatic species (e.g., precursor PAHs) also absorb in this range implying possible interference from semi-volatiles on the PTFE filters. However, given that the primary mechanism for PAH partitioning onto aerosols are by surface adsorption (Liang et al. 1997), on a mass basis it is expected that this is a small contribution. Second, the C = C atoms confined to a graphitic carbon lattice (e.g., as stacked graphene planes) have very few symmetry-allowed transitions in the mid-infrared (Kim et al. 2005; Kostić et al. 2009; Kuhlmann et al. 1998). Moreover, even in the perturbed ("turbostratic") morphology of soot carbon, it is unlikely that the symmetry conditions are relaxed such that this *particular* lattice vibration at ~1585 cm^{-1} is experimentally observed in transmission spectra (Andreae and Gelencsér 2006; Lechner et al. 2016). For example, only a very weak and broad C = C stretch is observed in the transmission spectra of graphite (ground under vacuum) even with areal densities are on the order of ~1000 μg-EC/cm^2 (Smith et al. 1975). CSN PTFE filters contain roughly ~1 μg-EC/cm^2. However, the infrared investigation of single-walled carbon nanotubes (SWNTs), activated carbons, and flame-derived soot demonstrate that oxidation introduces defects into elemental carbons, breaking ring symmetries and enhancing C = C absorption between 1620 cm^{-1} and 1580 cm^{-1} (Akhter et al. 1985a; Figueiredo et al. 1999; Kirchner et al. 2000; Kuznetsova et al. 2000; Mawhinney et al. 2000; Hamon et al. 2001; Galvez et al. 2002). Enhancement is particularly dramatic when heteroatom substituents are conjugated to phenyl rings (Smith and Chughtai 1995; Mayo 2004b). Considering the inherently weak absorption of defect-free elemental carbons coupled with low areal density of EC on these samples, absorption between 1600 and 1591 cm^{-1} is probably related to C = C bonds conjugated to oxygen or nitrogen-containing substituents. Since the features between 1657 and 1644 cm^{-1} were used for calibration and likely assignable to ring-conjugated C = O groups (e.g., possibly surface quinone defects), this lends credence to our hypothesis (Wexler 1967; Jang and McDow 1997; Olariu et al. 2002). Again, the limited molecular selectivity of FT-IR prevents assigning the stretching between 1600 and 1590 cm^{-1} exclusively to either soot or PAH derivatives, a fact not lost on other experimenters (Clague et al. 1999; Santamaría et al. 2006). These limitations apply to the tentatively assigned C = C aromatics stretches at 1615 cm^{-1} as well.

Finally, several weak PTFE combination bands are present in these CSN spectra in key regions (Liang and Krimm 1956; Brown 1964). Although it is often customary to ignore overtone and combination bands, the absorption of many PTFE fundamentals is on the order of 1–3AU or roughly 2–4 orders of magnitude larger than those of aerosol carbon. Considering this, we hypothesize that the single wavenumber from a well-resolved PTFE band at 1780 cm^{-1} (~0.015AU) serves to adjust PLS regression coefficients for positive interference from PTFE bands at ~1640 cm^{-1} and ~1590 cm^{-1}.

3.2. Infrared band assignments for atypical calibration

Figure 5 shows that the atypical EC calibration utilized very few wavenumbers for calibration, mostly aliphatic C-H stretching between 3000 and 2680 cm^{-1} (18 of the 27 wavenumbers). Aliphatic C-H stretches calibrated to atypical spectra were centered at 2970 cm^{-1} and 2926 cm^{-1} which correspond to CH_3 and CH_2 antisymmetric stretches, respectively (Shurvell 2002). Stretches at 2915 cm^{-1} have been identified in combustion soot and tentatively assigned to either C-H stretching in tertiary (methine) carbons or as possibly related to symmetric CH_2 Fermi resonance bands (Lu et al. 2005; Russo et al. 2014). The C-H stretching of aldehydes and/or O-CH_3 (methoxy) functional groups are tentatively assigned to features at 2750 cm^{-1} and 2687 cm^{-1}. Unlike the typical calibration no aromatic C-H stretches were used to model atypical EC. Notably, OH and NH groups as well as the C = C stretches (~1590 cm^{-1}) were also absent from the atypical calibration implying that atypical (Elizabeth, NJ) soot may show a lesser degree of oxidation.

Olariu et al. (2002) resolved a pattern of infrared absorption at ~1680 cm^{-1}, ~1630 cm^{-1}, and 1574 cm^{-1} in a product spectrum of *o*-, *m*-, and *p*-cresol photoxidation after subtracting the spectra of known products (e.g., 4-methyl-1,2-dihydroxybenzene). The resulting difference spectra were not identified with any particular standards but bands were assigned to either nitro (RNO_2) or organic nitrate ($RONO_2$) functional groups. Interestingly, the atypical EC calibration utilizes nearly this exact pattern of absorption. Therefore, we assign features at 1680 cm^{-1} to either quinone C = O stretches or possibly to R-ONO—the later identified in hexane soot at 1660 cm^{-1} (Smith and Chughtai 1995). Features at 1630 cm^{-1} and 1572 cm^{-1} are assigned to NO_2 antisymmetric stretching in $RONO_2$ and NO_2 antisymmetric stretching in RNO_2, respectively (Kirchner et al. 2000; Coates 2006). Other possible assignments include the C = O stretch of amides (1680 cm^{-1}) as well as the N-H bends of amines and/or particulate water at 1630–1625 cm^{-1} (Allen et al. 1994; Coates 2006).

3.2.1. Comparative analysis and interpretation of atypical behavior

Organic nitrogen functional groups appear as strong predictors of atypical (Elizabeth, NJ) EC and glaringly absent from the typical calibration. Notably, aerosols containing elevated quantities of diesel particulate matter (DPM) also contain elevated quantities of co-emitted organic nitrogen in the form of nitrated PAHs (NPAHs), several of which are used as DPM tracers (Zielinska et al. 2004; Schulte et al. 2015). Geographically, the Elizabeth, NJ monitoring station resides next to a toll station on the New Jersey Turnpike which seems a likely source of DPM. Furthermore, other researchers have shown that filters heavily loaded with DPM and analyzed by the IMPROVE_A TOR protocol have much lower OC/EC and show minimal propensity for charring compared to other sources (Khan et al. 2012). For the CSN samples used in this work, the thermal/optical behavior of Elizabeth, NJ samples conforms to that of DPM: Figure 6 compares the

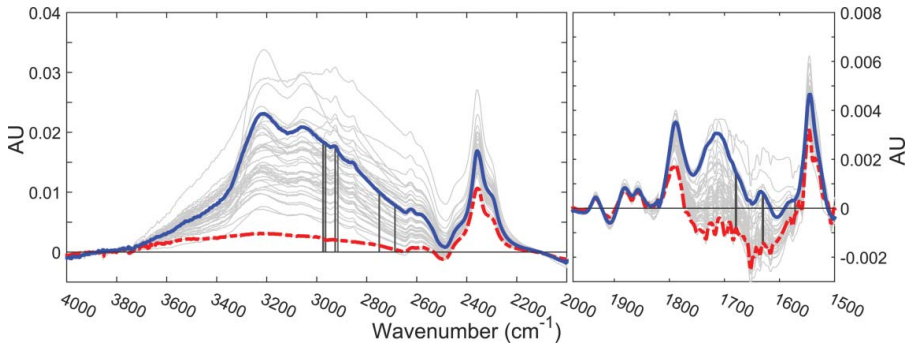

Figure 5. Atypical CSN spectra (light gray). A representative "typical" spectrum (solid line; blue), PTFE blank (dashes; red), and wavenumber used for calibration (vertical bars) are labeled. Thicker vertical bars indicate that several adjacent wavenumbers were chosen for calibration.

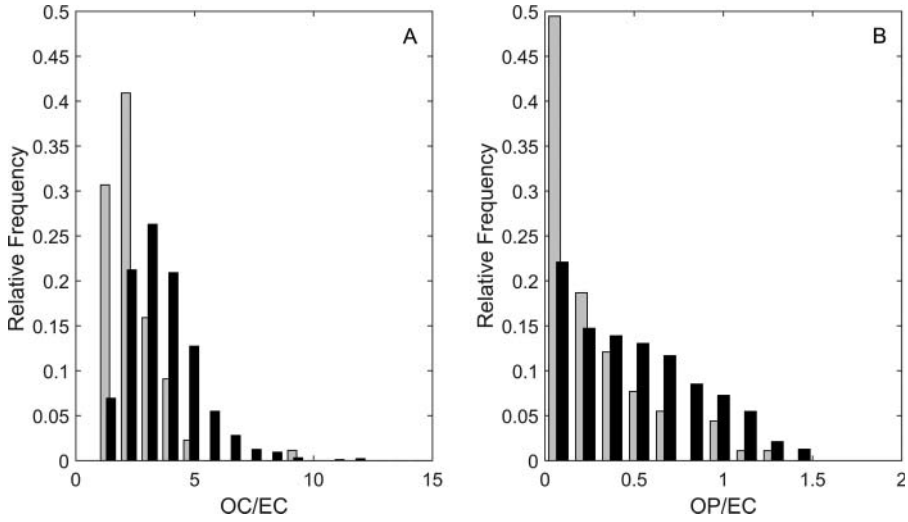

Figure 6. Distribution of OC/EC and OP/EC in Elizabeth, NJ samples (gray) and the other CSN sites (black).

distribution of Elizabeth, NJ OC/EC and OP/EC to those of the other eight sites. Specifically, OC/EC are lower on average in Elizabeth, NJ samples (mean OC/EC = 0.55 vs. 1.22), falling within the experimental uncertainty of the mean DPM OC/EC of an earlier study (Khan et al. 2012). Furthermore, Elizabeth, NJ samples exhibit minimal charring during TOR analysis with 76.9% of Elizabeth, NJ samples falling below the median char concentration (OP = 0.19 $\mu g/m^3$) and also show the lowest frequency of charring during TOR analysis (OP = 0 $\mu g/m^3$; 18% of samples). This is especially noteworthy given the relatively high mass-concentration of EC on NJ filters, motivating the comparison of OP/EC distributions between typical and atypical Elizabeth, NJ samples.

4. Conclusions

FT-IR EC has been predicted in fine aerosols from nine sites in the US Chemical Speciation Network. An initial single calibration developed from baseline-corrected FT-IR spectra determines EC on PTFE filters with unacceptable figures of merit (error and bias of 29% and 4%) when judged against previous IMPROVE network studies. Therefore, a formal multivariate classification procedure (PLS-DA) was used to allocate "atypical" spectra from Elizabeth, NJ and those containing a more "typical" CSN EC spectroscopic profile to their own dedicated calibrations. The result of independently predicting atypical and typical EC using a multilevel modeling framework improves the overall performance of the FT-IR method considerably, with CSN EC figures of merit closely reproducing IMPROVE EC figures. Reasons for the lower-than-anticipated R^2 of the multilevel EC model likely stems from the low-mass-per-unit area of EC on CSN filters.

The proximity of the Elizabeth, NJ sampler to a major toll station on the New Jersey turnpike as well as limited evidence of soot oxidation in infrared spectra further supported classifying Elizabeth samples as relatively atypical. The Elizabeth, NJ samples used to develop the atypical calibration were likely impacted by soot carbon sourced from fresh motor vehicle exhaust emissions. Elizabeth, NJ thermal-optical measurements, including the TOR pyrolysis artifacts (OP) and OC/EC distribution, were consistent with previous work that used IMPROVE_A protocol to speciate diesel particulate matter. This work demonstrates the principle of multilevel FT-IR EC modeling which may accommodate aerosol source differences across a broad range of samples within and outside the CSN.

This work extends the capability of FT-IR for rapid and non-destructive chemical characterization of PM using filters typically collected for standard gravimetric mass measurements. We demonstrate that the approach of Dillner and Takahama (2015a) for predicting TOR-equivalent EC is not limited to the IMPROVE network, but also the CSN network which has substantially lower areal mass density and PM with distinctly urban character. Furthermore, we demonstrate that our statistical calibrations can accommodate aerosols with diverse composition through a multilevel modeling framework. This approach would not be limited to TOR EC but can potentially be extended to other measurements such as BC or multiwavelength TOR, with FT-IR possibly providing additional insight into the most important infrared vibrations associated with new measurements as demonstrated here and previous work.

Acknowledgments

We thank the RTI International team for managing the CSN during the 2013 sampling year.

Funding

The authors acknowledge funding in cooperation with the U.S. EPA and the IMPROVE program (National Park Service cooperative agreement P11AC91045) and EPFL funding.

References

Akhter, M. S., Chughtai, A. R., and Smith, D. M. (1985a). The Structure of Hexane Soot I: Spectroscopic Studies. *Appl. Spectrosc.*, 39:143–153.

Akhter, M. S., Keifer, J. R., Chughtai, A. R., and Smith, D. M. (1985b). The Absorption Band at 1590 cm^{-1} in the Infrared Spectrum of Carbons. *Carbon*, 23:589–591.

Allen, D. T., Palen, E. J., Haimov, M. I., Hering, S. V., and Young, J. R. (1994). Fourier Transform Infrared Spectroscopy of Aerosol Collected in a Low Pressure Impactor (LPI/FTIR): Method Development and Field Calibration. *Aerosol Sci. Technol.*, 21:325–342.

Anderson, J. O., Thundiyil, J. G., and Stolbach, A. (2012). Clearing the Air: A Review of the Effects of Particulate Matter Air Pollution on Human Health. *J. Med. Toxicol.*, 8:166–175.

Andreae, M., and Gelencsér, A. (2006). Black Carbon or Brown Carbon? The Nature of Light-Absorbing Carbonaceous Aerosols. *Atmos. Chem. Phys.*, 6:3131–3148.

Arlot, S., and Celisse, A. (2010). A Survey of Cross-Validation Procedures for Model Selection. *Statist. Surv.*, 4:40–79.

Barker, M., and Rayens, W. (2003). Partial least Squares for Discrimination. *J. Chemom.*, 17:166–173.

Brown, R. G. (1964). Vibrational Spectra of Polytetrafluoroethylene: Effects of Temperature and Pressure. *J. Chem. Phys.*, 40:2900–2908.

Chen, K.-H., Lii, J.-H., Fan, Y., and Allinger, N. L. (2007). Molecular Mechanics (MM4) Study of Amines. *J. Comput. Chem.*, 28:2391–2412.

Chow, J. C., Watson, J. G., Chen, L.-W. A., Chang, M. O., Robinson, N. F., Trimble, D., and Kohl, S. (2007). The IMPROVE_A Temperature Protocol for Thermal/Optical Carbon Analysis: Maintaining Consistency With A Long-Term Database. *J. Air Waste Manag. Assoc.*, 57:1014–1023.

Chow, J. C., Watson, J. G., Pritchett, L. C., Pierson, W. R., Frazier, C. A., and Purcell, R. G. (1993). The DRI Thermal/Optical Reflectance Carbon Analysis System: Description, Evaluation and Applications in US Air Quality Studies. *Atmos. Environ., Part A*, 27:1185–1201.

Clague, A. D. H., Donnet, J. B., Wang, T. K., and Peng, J. C. M. (1999). A Comparison of Diesel Engine Soot With Carbon Black. *Carbon*, 37:1553–1565.

Coates, J. (2006). *Interpretation of Infrared Spectra, A Practical Approach, in Encyclopedia of Analytical Chemistry*. John Wiley & Sons, Ltd., New York, pp. 1–23.

Committee, A. M. (1987). Recommendations for the Definition, Estimation and Use of the Detection Limit. *Analyst*, 112:199–204.

Coury, C., and Dillner, A. M. (2008). A Method to Quantify Organic Functional Groups and Inorganic Compounds in Ambient Aerosols Using Attenuated Total Reflectance FTIR Spectroscopy and Multivariate Chemometric Techniques. *Atmos. Environ.*, 42:5923–5932.

Dillner, A. M., and Takahama, S. (2015a). Predicting Ambient Aerosol Thermal-Optical Reflectance (TOR) Measurements from Infrared Spectra: Organic Carbon. *Atmos. Meas. Tech.*, 8:1097–1109.

Dillner, A. M., and Takahama, S. (2015b). Predicting Ambient Aerosol Thermal-Optical Reflectance Measurements from Infrared Spectra: Elemental Carbon. *Atmos. Meas. Tech.*, 8:4013–4023.

Dixon, S. J., and Brereton, R. G. (2009). Comparison of Performance of Five Common Classifiers Represented as Boundary Methods: Euclidean Distance to Centroids, Linear Discriminant Analysis, Quadratic Discriminant Analysis, Learning Vector Quantization and Support Vector Machines, as Dependent on Data Structure. *Chemom. Intell. Lab. Syst.*, 95:1–17.

Figueiredo, J., Pereira, M., Freitas, M., and Orfao, J. (1999). Modification of the Surface Chemistry of Activated Carbons. *Carbon*, 37:1379–1389.

Fuzzi, S., Baltensperger, U., Carslaw, K., Decesari, S., Denier van der Gon, H., Facchini, M. C., Fowler, D., Koren, I., Langford, B., Lohmann, U., Nemitz, E., Pandis, S., Riipinen, I., Rudich, Y., Schaap, M., Slowik, J. G., Spracklen, D. V., Vignati, E., Wild, M., Williams, M., and Gilardoni, S. (2015). Particulate Matter, Air Quality and Climate: Lessons Learned and Future Needs. *Atmos. Chem. Phys.*, 15:8217–8299.

Galvez, A., Herlin-Boime, N., Reynaud, C., Clinard, C., and Rouzaud, J.-N. (2002). Carbon Nanoparticles from Laser Pyrolysis. *Carbon*, 40:2775–2789.

Gargiulo, V., Apicella, B., Alfè, M., Russo, C., Stanzione, F., Tregrossi, A., Amoresano, A., Millan, M., and Ciajolo, A. (2015). Structural Characterization of Large Polycyclic Aromatic Hydrocarbons. Part 1: The Case of Coal Tar Pitch and Naphthalene-Derived Pitch. *Energy Fuels*, 29:5714–5722.

Gundel, L. A., Dod, R. L., Rosen, H., and Novakov, T. (1984). The relationship Between Optical Attenuation and Black Carbon Concentration for Ambient and Source Particles. *Sci. Total Environ.*, 36:197–202.

Hallquist, M., Wenger, J., Baltensperger, U., Rudich, Y., Simpson, D., Claeys, M., Dommen, J., Donahue, N., George, C., and Goldstein, A. (2009). The Formation, Properties and Impact of secondary Organic Aerosol: Current and Emerging Issues. *Atmos. Chem. Phys.*, 9:5155–5236.

Hamon, M. A., Hu, H., Bhowmik, P., Niyogi, S., Zhao, B., Itkis, M. E., and Haddon, R. C. (2001). End-Group and Defect Analysis of Soluble Single-Walled Carbon Nanotubes. *Chem. Phys. Lett.*, 347:8–12.

Hand, J. L., Schichtel, B. A., Malm, W. C., and Frank, N. H. (2013). Spatial and Temporal Trends in PM2.5 Organic and Elemental Carbon across the United States. *Adv. Meteorol.*, 2013:13.

Hastie, T., Tibshirani, R., and Friedman, J. (2009). *The Elements of Statistical Learning: Data Mining, Inference, and Prediction*, 2nd ed. Springer New York, New York, NY.

Huntzicker, J., Johnson, R., Shah, J., and Cary, R. (1982). *Analysis of Organic and Elemental Carbon in Ambient Aerosols by a Thermal-Optical Method, in Particulate Carbon*. Springer, New York, pp. 79–88.

Jang, M., and McDow, S. R. (1997). Products of Benz[*a*]anthracene Photodegradation in the Presence of Known Organic Constituents of Atmospheric Aerosols. *Environ. Sci. Technol.*, 31:1046–1053.

Johnson, T. V. (2009). Review of Diesel Emissions and Control. *Int. J. Engine Res.*, 10:275–285.

Kanakidou, M., Seinfeld, J. H., Pandis, S. N., Barnes, I., Dentener, F. J., Facchini, M. C., Van Dingenen, R., Ervens, B., Nenes, A., Nielsen, C. J., Swietlicki, E., Putaud, J. P., Balkanski, Y., Fuzzi, S., Horth, J., Moortgat, G. K., Winterhalter, R., Myhre, C. E. L., Tsigaridis, K., Vignati, E., Stephanou, E. G., and Wilson, J. (2005). Organic Aerosol and Global Climate Modelling: A Review. *Atmos. Chem. Phys.*, 5:1053–1123.

Khan, B., Hays, M. D., Geron, C., and Jetter, J. (2012). Differences in the OC/EC Ratios that Characterize Ambient and Source Aerosols Due to Thermal-Optical Analysis. *Aerosol Sci. Technol.*, 46:127–137.

Kim, U. J., Furtado, C. A., Liu, X., Chen, G., and Eklund, P. C. (2005). Raman and IR Spectroscopy of Chemically Processed Single-Walled Carbon Nanotubes. *J. Am. Chem. Soc.*, 127:15437–15445.

Kirchner, U., Scheer, V., and Vogt, R. (2000). FTIR Spectroscopic Investigation of the Mechanism and Kinetics of the Heterogeneous Reactions of NO_2 and HNO_3 with Soot. *J. Phys. Chem. A*, 104:8908–8915.

Kostić, R., Mirić, M., Radić, T., Radović, M., Gajić, R., and Popović, Z. (2009). Optical Characterization of Graphene and Highly Oriented Pyrolytic Graphite. *Acta Phys. Pol., A*, 116:718–721.

Kroll, J. H., Lim, C. Y., Kessler, S. H., and Wilson, K. R. (2015). Heterogeneous Oxidation of Atmospheric Organic Aerosol: Kinetics of Changes to the Amount and Oxidation State of Particle-Phase Organic Carbon. *J. Phys. Chem. A*, 119:10767–10783.

Kroll, J. H., and Seinfeld, J. H. (2008). Chemistry of Secondary Organic Aerosol: Formation and Evolution of Low-Volatility Organics in the Atmosphere. *Atmos. Environ.*, 42:3593–3624.

Kuhlmann, U., Jantoljak, H., Pfänder, N., Bernier, P., Journet, C., and Thomsen, C. (1998). Infrared Active Phonons in Single-Walled Carbon Nanotubes. *Chem. Phys. Lett.*, 294:237–240.

Kuzmiakova, A., Dillner, A. M., and Takahama, S. (2016). An Automated Baseline Correction Protocol for Infrared Spectra of Atmospheric Aerosols Collected on Polytetrafluoroethylene (Teflon) Filters. *Atmos. Meas. Tech.*, 9:2615–2631.

Kuznetsova, A., Mawhinney, D. B., Naumenko, V., Yates, J. T., Liu, J., and Smalley, R. E. (2000). Enhancement of Adsorption Inside of Single-Walled Nanotubes: Opening the Entry Ports. *Chem. Phys. Lett.*, 321:292–296.

Lack, D. A., Mossmüller, H., McMeeking, G. R., Chakrabarty, R. K., and Baumgardner, D. (2014). Characterizing elemental, equivalent black, and refractory black carbon aerosol particles: a review of techniques, their limitations and uncertainties. *Analytical and Bioanalytical Chemistry*, 406(1): 99–122.

Lechner, C., Pannier, B., Baranek, P., Forero-Martinez, N. C., and Vach, H. (2016). First-Principles Study of the Structural, Electronic, Dynamic, and Mechanical Properties of HOPG and Diamond: Influence of Exchange–Correlation Functionals and Dispersion Interactions. *J. Phys. Chem. C*, 120:5083–5100.

Liang, C., and Krimm, S. (1956). Infrared Spectra of High Polymers. III. Polytetrafluoroethylene and Polychlorotrifluoroethylene. *J. Chem. Phys.*, 25:563–571.

Liang, C., Pankow, J. F., Odum, J. R., and Seinfeld, J. H. (1997). Gas/Particle Partitioning of Semivolatile Organic Compounds To Model Inorganic, Organic, and Ambient Smog Aerosols. *Environ. Sci. Technol.*, 31:3086–3092.

Lu, R., Gan, W., Wu, B.-h., Zhang, Z., Guo, Y., and Wang, H.-f. (2005). C−H Stretching Vibrations of Methyl, Methylene and Methine Groups at the Vapor/Alcohol ($n = 1-8$) Interfaces. *J. Phys. Chem. B*, 109:14118–14129.

Malm, W. C., and Hand, J. L. (2007). An Examination of the Physical and Optical Properties of Aerosols Collected in the IMPROVE Program. *Atmos. Environ.*, 41:3407–3427.

Massabò, D., Caponi, L., Bove, M. C., and Prati, P. (2016). Brown carbon and thermal-optical analysis: A correction based on optical multi-wavelength apportionment of atmospheric aerosols. *Atmos. Environ.*, 125:119–125.

Mawhinney, D. B., Naumenko, V., Kuznetsova, A., Yates Jr, J. T., Liu, J., and Smalley, R. E. (2000). Surface Defect Site Density on Single Walled Carbon Nanotubes by Titration. *Chem. Phys. Lett.*, 324:213–216.

Mayo, D. W. (2004a). *Characteristic Frequencies of Alkanes, in Course Notes on the Interpretation of Infrared and Raman Spectra*. John Wiley & Sons, Inc., New York, pp. 33–72.

Mayo, D. W. (2004b). *Characteristic Frequencies of Aromatic Compounds (Group Frequencies of Arenes), in Course Notes on the Interpretation of Infrared and Raman Spectra*. John Wiley & Sons, Inc., New York, pp. 101–140.

McDade, C. E., Dillner, A. M., and Indresand, H. (2009). Particulate Matter Sample Deposit Geometry and Effective Filter Face Velocities. *J. Air Waste Manag. Assoc.*, 59:1045–1048.

Næs, T., and Mevik, B.-H. (2001). Understanding the Collinearity Problem in Regression and Discriminant Analysis. *J. Chemom.*, 15:413–426.

Novakov, T., and Rosen, H. (2013). The Black Carbon Story: Early History and New Perspectives. *Ambio*, 42:840–851.

Olariu, R. I., Klotz, B., Barnes, I., Becker, K. H., and Mocanu, R. (2002). FT–IR Study of the Ring-Retaining Products from the Reaction of OH Radicals With Phenol, *o*-, *m*-, and *p*-Cresol. *Atmos. Environ.*, 36:3685–3697.

Petzold, A., Ogren, J. A., Fiebig, M., Laj, P., Li, S.-M., Baltensperger, U., Holzer-Popp, T., Kinne, S., Pappalardo, G., Sugimoto, N., Wehrli, C., Wiedensohler, A., and Zhang, X.-Y. (2013). Recommendations for reporting "black carbon" measurements. *Atmos. Chem. Phys.*, 13(16):8365–8379.

Pope III, C. A., and Dockery, D. W. (2006). Health Effects of Fine Particulate Air Pollution: Lines that Connect. *J. Air Waste Manag. Assoc.*, 56:709–742.

Pöschl, U. (2005). Atmospheric Aerosols: Composition, Transformation, Climate and Health Effects. *Angew. Chem. Int. Ed.*, 44:7520–7540.

Reggente, M., Dillner, A. M., and Takahama, S. (2016). Predicting Ambient Aerosol Thermal–Optical Reflectance (TOR) Measurements from Infrared Spectra: Extending the Predictions to Different Years and Different Sites. *Atmos. Meas. Tech.*, 9:441–454.

Russo, C., Stanzione, F., Tregrossi, A., and Ciajolo, A. (2014). Infrared Spectroscopy of Some Carbon-Based Materials Relevant in Combustion: Qualitative and Quantitative Analysis of Hydrogen. *Carbon*, 74:127–138.

Ruthenburg, T. C., Perlin, P. C., Liu, V., McDade, C. E., and Dillner, A. M. (2014). Determination of Organic Matter

and Organic Matter to Organic Carbon Ratios by Infrared Spectroscopy with Application to Selected Sites in the IMPROVE Network. *Atmos. Environ.*, 86:47–57.

Santamaría, A., Mondragón, F., Molina, A., Marsh, N. D., Eddings, E. G., and Sarofim, A. F. (2006). FT-IR and 1 H NMR Characterization of the Products of an Ethylene Inverse Diffusion Flame. *Combust. Flame*, 146:52–62.

Schulte, J. K., Fox, J. R., Oron, A. P., Larson, T. V., Simpson, C. D., Paulsen, M., Beaudet, N., Kaufman, J. D., and Magzamen, S. (2015). Neighborhood-Scale Spatial Models of Diesel Exhaust Concentration Profile Using 1-Nitropyrene and Other Nitroarenes. *Environ. Sci. Technol.*, 49:13422–13430.

Shindell, D., Kuylenstierna, J. C. I., Vignati, E., van Dingenen, R., Amann, M., Klimont, Z., Anenberg, S. C., Muller, N., Janssens-Maenhout, G., Raes, F., Schwartz, J., Faluvegi, G., Pozzoli, L., Kupiainen, K., Höglund-Isaksson, L., Emberson, L., Streets, D., Ramanathan, V., Hicks, K., Oanh, N. T. K., Milly, G., Williams, M., Demkine, V., and Fowler, D. (2012). Simultaneously Mitigating Near-Term Climate Change and Improving Human Health and Food Security. *Science*, 335:183–189.

Shurvell, H. (2002). *Spectra–Structure Correlations in the Mid– and Far–Infrared, in Handbook of Vibrational Spectroscopy*. John Wiley & Sons, Ltd., Chichester, pp. 1783–1816.

Smith, D. M., and Chughtai, A. R. (1995). The Surface Structure and Reactivity of Black Carbon. *Colloid. Surf. A: Physicochem. Eng. Aspects*, 105:47–77.

Smith, D. M., Griffin, J. J., and Goldberg, E. D. (1975). Spectrometric Method for the Quantitative Determination of Elemental Carbon. *Anal. Chem.*, 47:233–238.

Solomon, P. A., Crumpler, D., Flanagan, J. B., Jayanty, R. K. M., Rickman, E. E., and McDade, C. E. (2014). U.S. National PM2.5 Chemical Speciation Monitoring Networks—CSN and IMPROVE: Description of Networks. *J. Air Waste Manag. Assoc.*, 64:1410–1438.

Takahama, S., Ruggeri, G., and Dillner, A. M. (2016). Analysis of Functional Groups in Atmospheric Aerosols by Infrared Spectroscopy: Sparse Methods for Statistical Selection of Relevant Absorption Bands. *Atmos. Meas. Tech. Discuss.*, 2016:1–42.

Takahama, S., Johnson, A., and Russell, L. M. (2013). Quantification of Carboxylic and Carbonyl Functional Groups in Organic Aerosol Infrared Absorbance Spectra. *Aerosol Sci. Technol.*, 47:310–325.

Watson, J. G. (2002). Visibility: Science and Regulation. *J. Air Waste Manag. Assoc.*, 52:628–713.

Weakley, A., Miller, A., Griffiths, P., and Bayman, S. (2014). Quantifying Silica in Filter-Deposited Mine Dusts Using Infrared Spectra and Partial Least Squares Regression. *Anal. Bioanal. Chem.*, 406:4715–4724.

Weakley, A. T., Takahama, S., and Dillner, A. M. (2016). Ambient Aerosol Composition by Infrared Spectroscopy and Partial Least-Squares in the Chemical Speciation Network: Organic Carbon with Functional Group Identification. *Aerosol Sci. Technol.*, 50:1096–1114.

Wexler, A. S. (1967). Integrated Intensities of Absorption Bands in Infrared Spectroscopy. *Appl. Spectrosc. Rev.*, 1:29–98.

Wold, S., Sjöström, M., and Eriksson, L. (2001). PLS-Regression: A Basic Tool of Chemometrics. *Chemom. Intell. Lab. Syst.*, 58:109–130.

Zhao, Y., Zhang, J., and Nielsen, C. P. (2013). The Effects of Recent Control Policies on Trends in Emissions of anthropogenic Atmospheric Pollutants and CO_2 in China. *Atmos. Chem. Phys.*, 13:487–508.

Zielinska, B., Sagebiel, J., McDonald, J. D., Whitney, K., and Lawson, D. R. (2004). Emission Rates and Comparative Chemical Composition from Selected In-Use Diesel and Gasoline-Fueled Vehicles. *J. Air Waste Manag. Assoc.*, 54:1138–1150.